OPEN ACCESS
JOURNAL OF ADVANCED DIELECTRICS
Vol. 10, No. 6 (2020) 2050033 (12 pages)

DOI: 10.1142/S2010135X20500332

西安交通大學 XI'AN JIAOTONG UNIVERSITY

World Scientific
www.worldscientific.com

Bismuth zinc niobate: BZN-BT, a new lead-free $BaTiO_3$-based ferroelectric relaxor?

Jessica Marshall*, David Walker and Pam Thomas

Department of Physics, University of Warwick, Gibbet Hill Road, Coventry, CV4 7AL, UK

*j.marshall.4@warwick.ac.uk

Received 14 September 2020; Revised 18 November 2020; Accepted 21 November 2020; Published 23 December 2020

The novel lead-free ferroelectric relaxor system $x(Bi(Zn_{2/3}\ Nb_{1/3})O_3)(1-x)BaTiO_3$ (xBZN(1–x)BT) has received interest as a high-capacity relaxor dielectric material. Small quantities (< 10.0 mol.%) of BZN-based dopant had significant impacts on the structure of the $BaTiO_3$ host. This study evaluates the effect of BZN additions to the $BaTiO_3$ host up to xBZN = 10.0%. Initial additions of BZN were observed to stabilize tetragonal and orthorhombic coexistence at 295 K, alongside increasing dielectric constant. Peak dielectric constant and polarization were observed at $x < 4.0\%$, coinciding with maximum orthorhombic intensity and a local minima in tetragonal intensity. Compositions $0 < x < 4.0\%$ showed increasing polarization and a drop in T_m and classical ferroelectric properties. No significant dielectric dispersion was observed for compositions $x < 4.0\%$ over the frequency range 5–640 kHz. Compositions at $x > 4.0\%$ showed the onset of dielectric relaxation alongside a drop in polarization coincident with a drop in the tetragonal c_T/a_T ratio and the onset of the cubic phase at 295 K. Peak piezoelectric, dielectric and polarization values occurred over the range $3.8\% < x < 4.0\%$, alongside maximum orthorhombic intensity. Subsequent BZN additions showed a rapid onset of dielectric relaxation, alongside an increase in cubic intensity and a continuous drop in T_m with a minima near $x = 7.0\%$. Tetragonal presence at 295 K also vanished to zero at $x = 7.0\%$. Polarization loops ceased showing ferroelectric characteristics at $x > 5.0\%$, showing a transition from lossy relaxor dielectric to low-loss relaxor dielectric at $x > 10.0\%$.

Keywords: Relaxors; lead-free ferroelectrics; crystallography; piezoelectrics; dielectrics.

1. Introduction

The properties of relaxor ferroelectrics make them useful for a variety of applications including low-loss high-power dielectrics, energy storage, electrocaloric and nonlinear optical properties.[1–3] Other characteristics of relaxors are a diffuse dielectric maxima, ε_m and T_m ($T_m = T_c$ for classical ferroelectrics), a frequency-dependent ε_m, slim hysteresis loops and low values of E_c. In classical ferroelectrics, the free energy from the spontaneous polarization at temperatures, $T < T_c$ is minimized by the formation of ferroelectric domain walls typically 10–100 nm in diameter, with the dielectric constant having a discontinuity at $T = T_c$ with no significant frequency dispersion.

For relaxors, the temperature at the dielectric maximum, T_m, does not necessarily correspond to a phase change from long-range ferroelectric order to a centrosymmetric paraelectric phase.[1] Relaxors are characterized by the presence of microscopic clusters a few unit cells in size known as polar nanoregions (PNRs),[1,4,5,6] which form on cooling through the Burns temperature (T_d). PNRs are initially a few unit cells in diameter and are generally a lower symmetry phase than the ferroelectric host, which is usually still paraelectric at $T = T_d$. Near T_d, the dipoles are weakly coupled and are free to reorient in the presence of random electric fields, resulting in an apparently paraelectric structure for typical diffraction coherence length scales (~ 1 μm) at $T > T_m$. With decreasing temperature, PNRs exhibit enhanced coupling resulting in an increase in long-range order and a decrease in their dynamic character. Near T_m, a ferroelectric state can be induced by the application of an electric field greater than the critical field, E_c. Relaxor ferroelectrics at $T < T_m$ can exhibit typical ferroelectric properties and exhibit frequency dispersion (significant $\Delta\varepsilon_m$ and ΔT_m with probe frequency at the dielectric peak) around T_m. Coexistence of paraelectric and ferroelectric phases near T_m can also occur.[1,6] The structural disorder present within relaxors means that multiple polar phases can coexist at $T < T_m$, and this often enhances key ferroelectric properties including piezoelectric coefficients and coupling factors.[6–8]

Relaxor additives are commonly added to classical ferroelectric solid solutions, e.g., bismuth zinc niobate — lead titanate ($Bi(Zn_{2/3}\ Nb_{1/3})O_3$ — $PbTiO_3$), (BZN-PT).[9] Nomura *et al.*[9] observed that additions of $Bi(Zn_{2/3}\ Nb_{1/3})O_3$) (BZN) to $PbTiO_3$ had greater tetragonality than $PbTiO_3$, alongside increasing T_c. Paterson[10] followed on from this work by adding $Bi(Zn_{2/3}\ Nb_{1/3})O_3$ to $BaTiO_3$ as a lead-free analogue of BZN-PT and noted that tetragonality reduced with BZN additions. Further work[2,3,11] also observed decreasing tetragonality with subsequent BZN additions, with the system assuming a pseudocubic appearance near x(BZN) = 5.0%[3,11] up to the miscibility limit at $x \leq 22.0\%$.[11]

Considerable changes to the structural and dielectric properties have been observed at low concentrations of BZN ($x \leq 4.0\%$) additions. $Bi(Zn_{2/3}\ Nb_{1/3})O_3$-$BaTiO_3$ (xBZN(1−x)BT) has been identified as a low-loss energy storage material[2,12] with BZN-doped BT (xBZN(1−x)BT) showing considerable structural disorder[11] with phase polymorphism present at small ($x < 5.0\%$) BZN additions. Ferroelectricity has also been observed in the (xBZN(1−x)BT) solution for $x \leq 5.0\%$.[2,11] This study investigated the structural and physical properties of dilute xBZN(1−x)BT ($0 < x < 10.0\%$) solutions using high-resolution powder X-ray diffraction (HRXRD), dielectric measurements and polarization switching on bulk ceramic samples.

2. Method

2.1. *Powder calcination*

The xBZN(1−x)BT precursors were prepared by making the end member precursors first. The $BaTiO_3$ precursor was prepared using $BaCO_3$ and TiO_2 (Sigma Aldrich 99.95%) by mixing for 24 h in isopropyl alcohol using zirconia media at a 10:1 media : charge ratio. Prior to mixing, $BaCO_3$ and TiO_2 were dried for 1 h in air at 573 K to remove adsorbed water.[13] The $Bi(Zn_{2/3}\ Nb_{1/3})O_3$ precursor was prepared as for $BaTiO_3$ by heating to 573 K prior to mixing as for $BaTiO_3$. BZNBT precursor powders were mixed by adding stoichiometric quantities of BZN to $BaTiO_3$ precursors in initial steps of 1 mol.% (metals basis)[11,13] with a uncertainty in mass measurement of ± 0.003 g. The $BaTiO_3$ and BZN precursors were made up to a maximum 20 g batches to minimize compositional uncertainty. Maximum uncertainty in composition was determined as (1 ± 0.05) mol.% for compositions $0 < x < 3.4\%$ and $5.0\% < x < 10\%$. Maximum uncertainty for compositions $3.4\% < x < 5.0\%$ was determined to be ± 0.032 mol.%.

DTA/TGA analysis was performed to determine suitable ramp rates and dwells for different BZN-BT compositions.[1,13] Precursors were calcined in platinum crucibles within closed alumina crucibles in air for 4 h at maximum dwell temperatures between 1128–1218 K. Post calcining, powder was weighed to determine that precursor reactions had gone to completion prior to examination with XRD. Calcined powder was examined at room temperature using a Bruker D5005 diffractometer with Cu K_α radiation over a range of 20°–90° 2θ. The calcined powder was > 99% phase pure with small quantities of secondary phases identified mostly as $BaTi_2O_5$ (PDF 04-012–4418). Calcined precursors were milled with zirconia media with a 10:1 media: charge ratio in IPA for a further 20 h to ensure compositional homogeneity and crystallite size prior to sintering.

2.2. *Powder standard preparation and characterization*

Sintered powder specimens for high-resolution X-ray diffraction were prepared from calcined powder precursors. Precursors were crystallized by heating in air in closed platinum crucibles between 1463–1513 K for a 2 hhot dwell, with 2–3 g powder used per charge. Post crystallization, the powder mass was de-agglomerated, sieved (100 μm mesh) and annealed in air for 2 h at 473 K prior to HRXRD. Weight loss for all compositions was < 1% indicating no significant mass loss took place from the calcined precursors during sintering. HRXRD was performed at 295 K using a Panalytical X'pert Pro MPD diffractometer equipped with a curved Johansson (Ge(111)) monochromator giving focused Cu $K_{\alpha 1}$ radiation. A solid state Pixcel detector was used with a step size of ~0.013° and a range of 20–135° 2θ with a total scan time of 15 h. Peaks were identified using Panalytical High Score Plus software and the latest ICDD PDF 4+ database.

Rietveld refinement was performed using the TOPAS Academic 6 Rietveld refinement software (Pearson VII peak fitting model), including atomic displacement and thermal parameters. Best fits were obtained using anisotropic displacement parameters (ADPs) for polar phases. Isotropic displacement parameters were only used for the cubic phase as use of ADPs caused the cubic models to become unstable during refinement.

Restraints on the lattice parameters were based on those by Wu *et al.*[11] for the initial refinements. The tetragonal xBZN(1−x)BT phase was fitted using a modified version of the $BaTiO_3$ PDF as the baseline (PDF 00-005 0626, *P*4 mm). Models for orthorhombic xBZN(1−x)BT were based on the PDF 01-083-8301 for $BaTiO_3$ *Amm2*. The sintered powder xBZN(1−x)BT standards were composed of > 99% phase pure xBZN(1−x)BT, with the parasitic phases identified as $BaTi_2O_5$ (PDF 00-008-0368) and $Ba_6Ti_{17}O_{40}$ (PDF 00-026-0321).

2.3. *Ceramic preparation and microscopy*

Ceramic samples were prepared using the de-agglomerated calcined precursors as described in Sec. 2.1. Cylindrical pellets of green dimensions approximately 13 mm diameter × 2.7 mm thickness were pressed at 80 MPa with 0.01 ml of 2 wt.% aqueous PVA solution as the organic binder. Samples were sintered in a sealed platinum crucible within a powder bed consisting of calcined 0.2BZN(1−x)0.8BT to counter Bi_2O_3 loss. An inner layer of powder of the same sample composition adjacent to the pellet prevented contamination between the BZN-enriched outer powder bed and pellets. Pressed pellets, following an organic de-binding step for 1 h at 923 K then ramped at 10 K min^{-1} were then sintered between 1463–1553 K for 90–120 min for the hot dwell, then cooling at 0.5 K min^{-1} for 30 K prior to an isothermal hold between 15–60 min, until cooling at 2 K min^{-1} to room temperature. Sintered density was assessed using the Archimedes method with a modified Precisa balance and the theoretical density calculated from lattice parameters determined from powder standards. Dense (≥95%) ceramics were polished with silicon carbide paper and Struers diamond suspension

on polishing cloth down to 1 μm to an average thickness of 1 mm. Conductive silver paint electrodes were painted on the polished faces and annealed at 773 K for 1 h prior to measurement.

2.4. *Dielectric measurements*

Dielectric measurements were obtained using a Hewlett Packard 4192A impedance analyzer. Capacitance and dielectric loss were measured using a 1.1V sin wave over the frequency range 5–640 kHz up to 650 K. Conductance was measured from room temperature up to 500 K from 5 kHz to 56.5 kHz. Polarization measurements were performed using an aixACCT TF Analysis A3000 with a TREK high voltage amplifier, enabling a maximum voltage of ± 2 kV (= 20 kV cm^{-1}) for 1 mm thick ceramic samples. Polarization (*P*–*E*) loops and current-voltage curves were measured at a frequency of 1 Hz at ambient temperature (295 K). Average remnant polarization P_r is defined as $P_{r,\text{average}} = (P_{r+} + |P_r-|)/2$. Spontaneous polarization P_s is determined by a linear fit of the first 10 points from the maximum polarization P_{sat} to closely approximate the tangent on the curve of the *P*–*E* loop from which P_s is defined.

Measurements of d_{33} were obtained using a YE2730A d_{33} meter (APC International) with a quartz standard for calibration. Prior to measurements, an applied voltage equivalent to twice the coercive field E_c (as determined from polarization data, range 2.0–3.0 kV) was applied to samples via Pt wire electrodes in silicone oil at 295 K. Voltage was applied to each sample for 3 min to ensure stability of electric field and that the samples were fully poled. Samples were measured at a variety of locations on the surface and on both sides to ensure validity of results and to ascertain measurement uncertainty.

3. Results

3.1. *HRXRD spectra at 295K*

Figure 1(a) shows a general overview of the *x*BZN(1–*x*)BT system with XRD spectra showing at least two phases present from the emergence of a third peak in the middle of the (002)/$(200)_T$ doublet at $x \geq 2.0\%$. This additional peak showed the best correspondence to the (200)/$(022)_O$ peak attributed to the space group *Amm2* (Orthorhombic lattice parameters, $a_O \approx (a_T + c_T)/2$, $b_O \approx a_O*\sqrt{2} \approx c_O$), appearing between the resolved $(002)_T$ and $(200)_T$ peaks from the tetragonal doublet. The (200)/$(022)_O$ peak increases in intensity as *x* increases, reaching a maximum near $x = 4.0\%$. At $x = 4.0\%$, the diffracted intensity of the (200)/$(022)_O$ attributed to *Amm2* shows a sharp drop in intensity, whereas the *P*4 mm $(002)_T$ and $(200)_T$ shows a spike in intensity at $x = 4.0\%$. Diffraction patterns for compositions at $x > 4.0\%$ start to show a more pseudocubic structure with a drop in tetragonal intensity alongside the appearance of the paraelectric *Pm*-3*m* phase. For $x > 4.0\%$, the intensity attributed to *Amm2* stays roughly constant with increasing BZN additions.

This is consistent with the best fits ascribed to the appearance of the cubic *Pm*-3*m* phase at 295 K, first present as a trace at $x = 4.0\%$, and its rapid rise in associated diffracted intensity with subsequent BZN additions for $x > 4.0\%$.

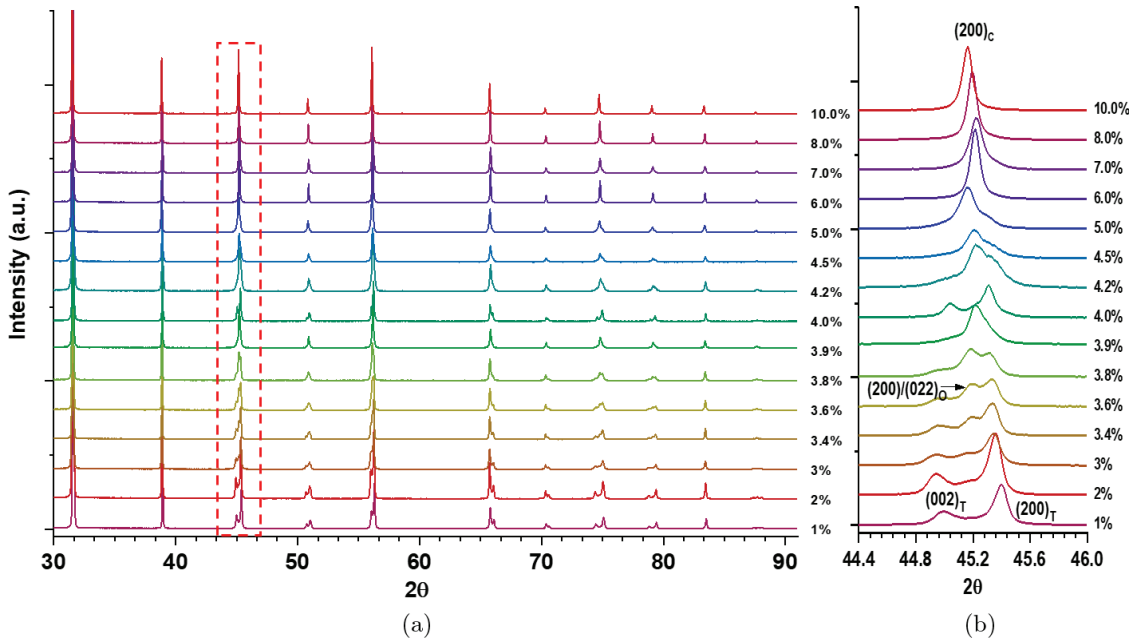

Fig. 1. (a) X-ray spectra for compositions with BZN additions in mol.% showing phase polymorphism at low BZN ($x < 5.0\%$) concentrations. The $(200)_c$ pseudocubic peak is shown in (b) showing the onset of a third peak near around $x = 3.0\%$.

Trends in diffracted intensity are broadly consistent with observations by Wu *et al.*[2,11] who observed the drop in tetragonality over $3.8\% < x \leq 4.0\%$ and the appearance of the pseudocubic phase at $x \geq 4.0\%$. Previous work on the xBZN(1–x)BT system[2,11] used a model with tetragonal and rhombohedral polar phases present between $3.4\% < x < 20.0\%$. However, no significant asymmetry of the (111) peak was observed at any composition at 295 K, which would be the case for any unit cell with a non 90° angle. Trends in diffracted intensity are consistent with observations by Wu *et al.*[2,11] who observed the drop in tetragonality near $x = 3.8\%$ and the appearance of the pseudocubic phase at $x \geq 4.0\%$.

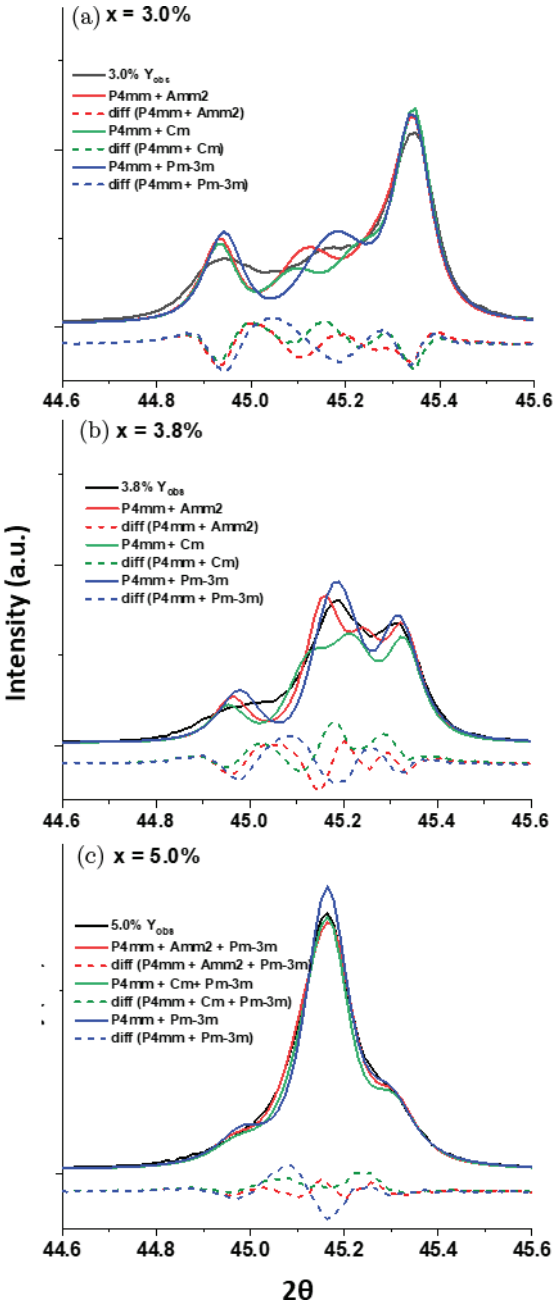

Fig. 2. Model fits for (a) x =3.0%, (b) x = 3.8% and (c) x = 5.0%. Models using *Amm2* had the most consistent fits over all compositions. Fits were generally poorer for compositions $x \leq 3.8\%$.

Models used for fitting used Amm2, Cm ($a_M \approx b_M \approx a_T*\sqrt{2}$, $c_M \approx a_T$, $\beta \approx 90°$) and *Pm-3m* alongside *P*4 mm for $3.0\% < x < 6.0\%$, since orthorhombic and monoclinic polar phases often coexist with a tetragonal polar phase.[14,15] Reasonable fits were obtained from the *P4mm* + *Pm-3m* and *P4mm* + *Cm*. The *P4mm* + *Amm2* (with *Pm-3m* present at $x > 4.0\%$) had the better fits from the GoF factor. For an ideal model the GoF will be as close to 1 as possible. Model fits over the $(200)_{pc}$ doublet for (a) $x = 3.0\%$, (b) $x = 3.8\%$ and (c) $x = 5.0\%$ are shown in Fig. 2:

Structural models comprised solely of polar phases (*P4mm*, *Cm* and *Amm2*) showed poorer fits to the observed intensity at $x \geq 4.0\%$ as shown in Fig. 2(c), particularly at high 2θ angles. The addition of a *Pm-3m* phase at $x \geq 4.0\%$ with $a_c \approx 4.014$ Å significantly improved the GoF and is consistent with sharp increase in the fraction of the cubic phase from $4.5\% < x < 8.0\%$.

The identity of the secondary polar phase was further investigated by comparing the GoF factor for models incorporating other possible symmetries alongside *P*4 mm, as found in other work.[1,16,17] The minimum expected Bragg factor, $R_{exp.}$[18] varied from $4.0\% < R_{exp} < 8.0\%$ over all compositions. The goodness-of-fit (GoF) parameter is defined as the ratio of the calculated Bragg factor R_{wp} to the expected Bragg factor R_{exp}, where GoF = $R_{wp}/R_{exp.}$[18,19] Trends of R_{wp}, R_{exp} and GoF are shown in Fig. 3.

Figure 3 shows that GoF factors for all models converge to a local minima at $x = 3.9\%$, indicating that the long-range structure at $x = 3.9\%$ has a pseudocubic appearance, despite being ferroelectric. The transition from tetragonal to orthorhombic phases, whether composition or temperature driven, has been observed in other relaxor ferroelectrics systems, including $1–x(Bi_{0.5}Na_{0.5})TiO_{3-}$ $xBaTiO_3$[16] and $(1–x)BaTiO_3$ – $xBiSnO_3$ system.[17]

Models using *Amm2* as the secondary polar phase as shown in Fig. 2, had consistently lower GoF than those with *Cm* or *Pm-3m*. This is evidence that the secondary polar phase is orthorhombic in basis, rather than monoclinic or rhombohedral. Trends in diffracted intensity attributed to *P*4 mm are broadly consistent with observations by Wu *et al.*[2,11] who observed the decline in tetragonality with BZN additions, resulting in a local minima at $3.8\% < x \leq 4.0\%$.

In the composition range $4.5\% < x < 8.0\%$. diffracted intensity attributed to *Amm2* remains mostly constant (~ 25% total intensity), while *P4mm* intensity steadily declines from ~35% at $x = 4.5\%$ to 0 at $x = 7.0\%$. For $7.0\% < x < 20.0\%$, *Amm2* intensity showed an asymptotic decrease to ~20% of total diffracted intensity near $x = 10.0\%$. Trends in phase abundance with composition up to $x = 10.0\%$ at room temperature are shown in Fig. 4.

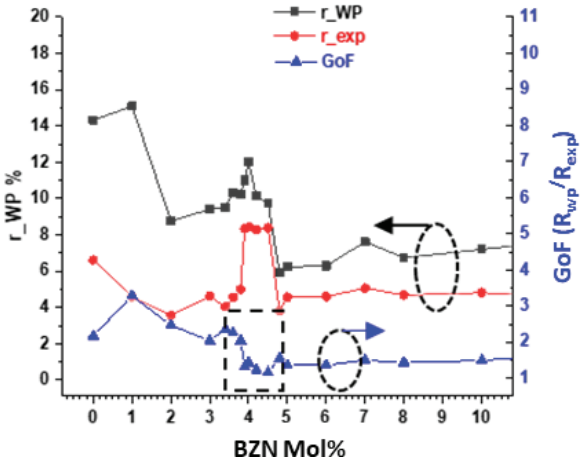

(a)

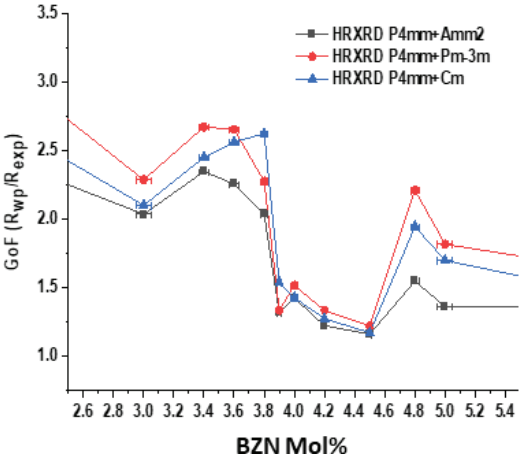

(b)

Fig. 3. (a) R_{wp}, R_{exp} and GoF for XRD models for compositions $0 < x < 10.0\%$. Increase in R_{exp} for compositions $3.8\% < x < 4.5\%$ is from reduced total counts relative to adjacent data. (b) Comparison of models with two polar phases (tetragonal and orthorhombic), (tetragonal and monoclinic) and tetragonal and cubic.

BZN additions have a significant impact on the crystal structure of the $BaTiO_3$ host as shown in Figs. 1 and 4, even at low concentrations such as $x = 1.0\%$, where the *Amm2* phase is stabilized at 295 K. Diffracted intensity ascribed to *Amm2* increased up to $x = 3.9\%$, prior to a rapid drop in intensity at $3.9\% < x < 4.0\%$. The drop in *Amm2* intensity coincides with the first appearance of trace cubic presence at 295 K at $x = 4.0\%$. The initial local maxima in *P4mm* at $x = 4.0\%$ is followed by a rapid decline, reaching zero near $x = 7.0\%$ alongside a corresponding increase in *Pm-3m* presence.

The discontinuity in diffracted intensity at $x = 4.0\%$ is reflected in the change in lattice parameters for the polar *P*4 mm and *Amm2* phases and the change in tetragonal c_T/a_T ratio in Fig. 5(a). From the known phase diagrams of $BaTiO_3$ and previous work on this system,[3,12,14] some of this instability indicates that phase transitions take place at or near room temperature, particularly for compositions $3.8\% < x < 5.0\%$.

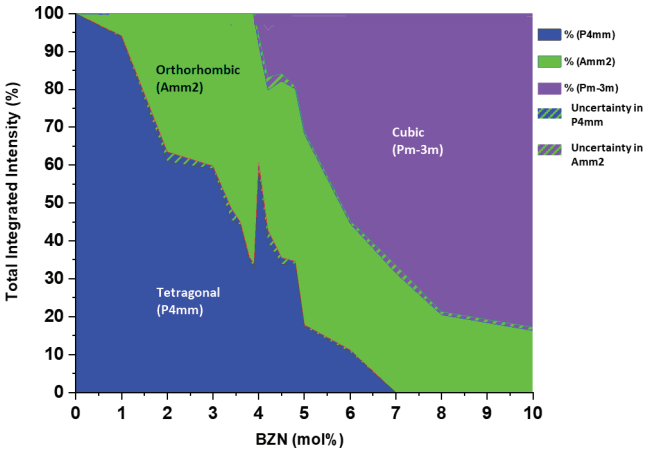

Fig. 4. Relative phase abundance for the BZNBT ferroelectric relaxor system at 295 K as determined by Rietveld refinement. Note the discontinuity in the orthorhombic/tetragonal abundance near $x = 4.0\%$ and trace cubic presence at 295 K at $x > 4.0\%$. Uncertainty in attributed intensity is shown in the hashed areas.

Such phase transitions as well as the possibility of a remnant low temperature *R*3*m* phase can be investigated by nonambient diffraction methods.

The decline in c_T/a_T ratio occurs over a much narrower compositional regime than observed in previous work on xBZN(1–x)BT[2,11] and shows a strong local minima at $x = 3.9\%$. Reasons for this are due in part to the high resolution of the diffractometer and the large number of high purity samples (5 discrete compositions for $3.6\% < x < 4.5\%$ inclusive) over the composition range $3.6\% < x < 4.5\%$ where previous studies of this system have identified dielectric maxima[11] and structural transitions[3,11] near $x = 4.0\%$. This enables a much higher resolution in terms of compositional accuracy and XRD measurements over the region near $x = 4.0\%$ compared to previous studies.

Figures 5(a) and 5(b) shows a convergence in lattice parameters for both *P4mm* and *Amm2* phases near $x = 4.0\%$. The $(111)_{pc}$ peak was evaluated to examine any asymmetry attributable to non90° angle within unit cells. In Figs. 5(c) and 5(d), the $(201)_{pc}$ peak was selected over the $(200)_{pc}$ doublet for FWHM and integrated intensity comparison, since the $(201)_{pc}$ better shows changes in orthorhombic intensity over $3.0\% < x < 6.0\%$ than $(200)_{pc}$.

The drop in FWHM and integrated intensity in Figs. 5(c) and 5(d) are also indicative of a general convergence in lattice parameters for both polar phases. Note that for $(111)_{pc}$, there is a sharp jump in FWHM at $x \geq 4.0\%$ which is driven by the jump in tetragonal intensity at $x = 4.0\%$. The drop in FWHM is evidence that the long-range *Amm2*-dominated xBZN(1–x)BT shows a pseudo-cubic-like structure at $3.8\% < x < 4.0\%$.

3.2. *Dielectric and conductivity measurements*

The relative permittivity and dielectric loss were measured from room temperature to 650 K between 5–640 kHz.

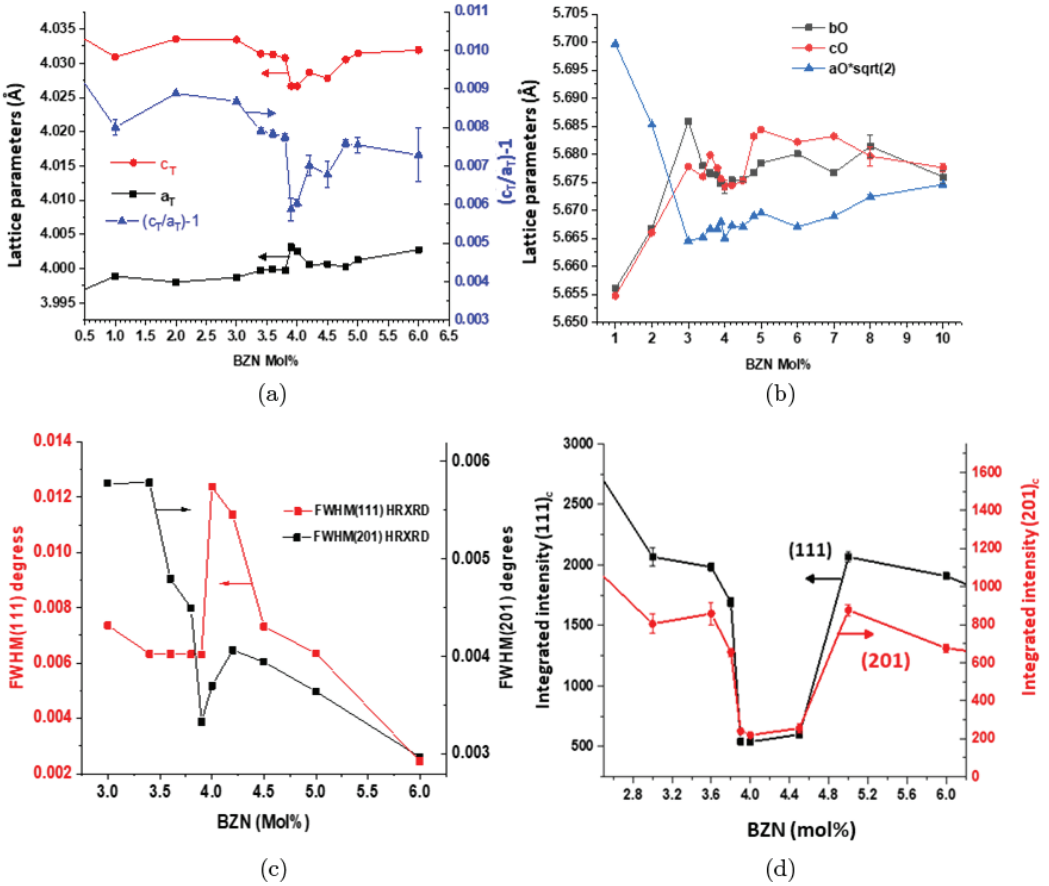

Fig. 5. Trends in lattice parameters with BZN composition for (a) tetragonal and (b) orthorhombic phases. The change in tetragonal ratio $((c_T/a_T) - 1)$ is shown in (a) alongside the c_T and a_T parameters with BZN content. (c) shows trends in FWHM from raw data for the $(111)_{pc}$ and $(201)_{pc}$ with composition and (d) Integrated intensities of $(111)_{pc}$ and $(201)_{pc}$ peaks showing local minima at $3.8\% < x < 5.0\%$.

Figure 6 summarizes ε_m, T_m and the dielectric dispersion recorded from all compositions, respectively.

Values of ε_m and T_m were measured from the capacitance measured from the Hewlett Pickard 4192A impedance analyzer with an uncertainty in temperature of ± 1 K and the nearest whole number for ε_m for each frequency. The magnitude of dielectric dispersion in peak temperature ΔT_m was determined from the difference between T_m at 5 kHz and T_m at 640 kHz. Similarly, $\Delta\varepsilon_m$ was calculated from the difference between ε_m at 5 kHz and ε_m at 640 kHz and given as a percentage of ε_m at 5 kHz for clarity. For compositions, where $T_m < 290$ K at 5 kHz (and hence ε_m), additional data has been interpolated from Wu *et al.*[11] Trends in ε_m, T_m and dispersion (ΔT_m and $\Delta\varepsilon_m$) are shown in Fig. 6.

In terms of the magnitude of the dielectric maximum ε_m, Paterson *et al.*[10] determined a maximum ε_m at $x = 5.0\%$ of 10,000 at 1 kHz. Conversely, Chen et al[3] identified $x = 2.0\%$ as the composition with the highest ε_m up to 60,000 for 10 kHz. More comprehensive studies on dielectric studies by Wu *et al.*[2,11] show maximum values of ε_m around 5000 over composition ranges $2.0\% < x < 6.0\%$. In this work, dielectric ε_m attains its highest overall value where $\varepsilon_m = 4846$ at 5 kHz for $x = 4.5\%$ and is high (> 3000) for compositions $3.0\% < x < 7.0\%$, which is more consistent with the studies by Wu *et al.*[2,11] Dielectric loss was observed to decrease initially with BZN addition to a minimum near $x = 4.0\%$, remaining low up to $x = 5.0\%$. The loss increases steeply at $x > 5.0\%$ with a maximum at $x = 8.0\%$, coinciding with the drop in ε_m and maximum dielectric and temperature dispersion. The dielectric loss subsequently decreases for further BZN additions at $x > 8.0\%$ with compositions $x > 10.0\%$ showing a dielectric loss consistent with low-loss relaxor dielectrics and previous studies of this system. Plots of dielectric constant and loss with temperature and composition are shown in Appendix A).

The temperature of the dielectric maxima T_m decreases continuously with BZN content, reaching a local minima near $x = 7.0$, where $T_m < 290$ K for ε_m (5 kHz), consistent with previous research indicating that minimum T_m is in the region $6.0\% < x < 8.0\%$.[10,11] Dielectric and temperature dispersion ΔT_m and $\Delta\varepsilon_m$ is negligible for $x \leq 3.9\%$ as seen in Fig. 6, but $\Delta\varepsilon_m$ increases rapidly with a maximum in relative and absolute $\Delta\varepsilon_m$ at $x = 4.5\%$ from its onset at $x \geq 4.0\%$, despite ΔT_m being relatively small at $x = 4.5\%$. Composition $x = 4.5\%$ shows considerable disorder compared to other relaxor

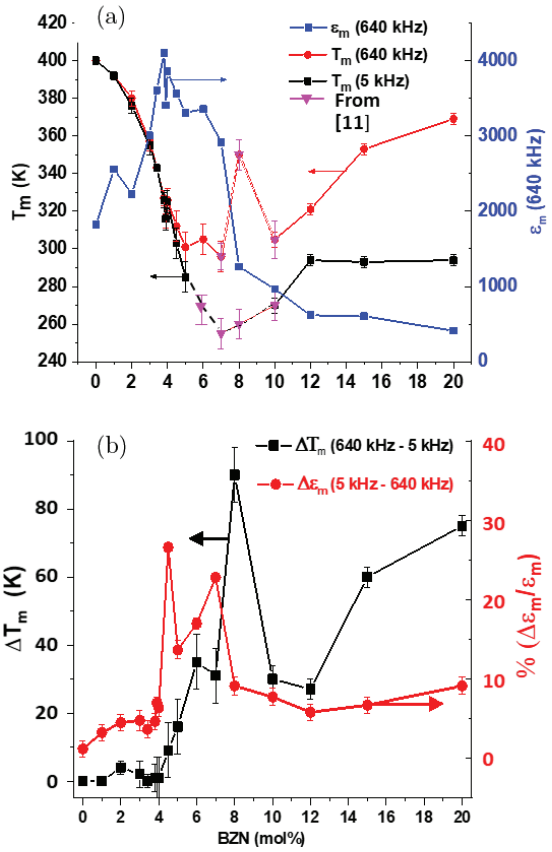

Fig. 6. (a) Plots of T_m and ε_m and (b) ΔT_m and normalized $\Delta\varepsilon_m$ with BZN concentration. Note the dielectric anomalies at $x = 4.5\%$ and 8.0%. Dotted lines at $x = 8.0\%$ in Fig. 6(a) indicate local maxima in T_m (640 kHz). ΔT_m and $\Delta\varepsilon_m$ in 6(b) calculated using interpolated data for $5.0\% < x < 10.0\%$ for 5kHz from Wu *et al.*[11]

compositions in that frequency and dielectric values do not show the usual trends of ε_m where ε_m typically decreases and T_m increases with increasing frequency — the standard relationship only holds for frequencies ≥ 80 kHz. Some of this could be due to the unusual dielectric properties of composition $x = 4.5\%$ but non-optimized processing conditions cannot be ruled out. This is particularly true when it is well known that grain size has significant impact on dielectric and piezoelectric properties.[20,21]

Overall, ΔT_m and normalized $\Delta\varepsilon_m$ increase steadily with additional BZN from $x > 4.5\%$, with ΔT_m reaching a maxima at $x = 8.0\%$, the trend in in T_m broadly consistent with previous investigations[2,11] of this system. ΔT_m and $\Delta\varepsilon_m$ decline at $x > 8.0\%$, with $\varepsilon_m \approx 500$ and $\Delta T_m \sim 60$ K for $x \geq 12.0\%$. Dielectric observations show that the xBZN(1–x)BT system has nondispersive ferroelectric characteristics up to $x = 3.9\%$ and shows a rapid transition to a lossy ferroelectric relaxor regimen at $4.0\% < x < 5.0\%$.

Conductance was measured between room temperature and 480 K between 5–6.6 kHz and is shown for selected compositions in Fig. 7. Conductance shows similar initial trends with composition as ε_m with peak conductance at T_m for $x < 4.0\%$. Some significant differences in temperature dependency are observed between the conductance and ε_m, specifically for $x = 1.0\%$ and $x = 2.0\%$. Both these compositions show large, broad peaks in conductance at $T < T_m$ and at T_m itself. These lower-temperature peaks are most likely due to the transition between an orthorhombic-dominant to a tetragonal-dominated structure, which occurs near 300 K for $x = 1.0\%$. For *Amm2*-dominated compositions $3.4\% < x < 4.0\%$, the peak conductance shows a sharp peak at T_m, relative to the broad peak for *P4mm*-dominated composition at $x = 1.0\%$ (Fig. 7(a)). At $x = 4.0\%$ in Fig. 6(d), peak conductivity does not coincide with T_m as it does for $x = 3.9\%$ (Fig. 6(c)) being the limit of peak conductivity at T_m. This is also coincident with the discontinuity in crystal structure near $x = 4.0\%$ shown in Figs. 1 and 4. The structural discontinuity revealed by XRD is also present in the electrical and dielectric properties of this system and shows a similarly sharp boundary between $3.9\% < x < 4.0\%$, as shown by Figs. 7(c) and 7(d). Further BZN additions show a shift in conductance to lower temperatures but since $T_m < 290$ K for $x > 5.0\%$ for probe frequencies ≤ 56.6 kHz the displacement between peak conductance, ε_m and T_m for $x > 5.0\%$ is unclear.

3.3. *Piezoelectric data*

The average direct piezoelectric coefficient d_{33} was observed to increase with BZN additions up a maximum near $x = 3.9\%$, as shown in Fig. 8, alongside the tetragonality ratio $(c_T/a_T) - 1$. No significant d_{33} response at 295 K was detected for compositions $x > 5.0\%$.

The increase in d_{33} was initially independent of c_T/a_T ratio up to $x = 3.0\%$ where at $3.0\% < x < 3.9\%$ an inverse correlation between d_{33} and $(c_T/a_T) - 1$ is observed, the peak in d_{33} coinciding with the local minima in c_T/a_T and tetragonal intensity at $x = 3.9\%$. Values of d_{33} drop sharply at $x \geq 4.0\%$ in line with a sharp spike in tetragonal intensity, but the c_T/a_T ratio does not start to decrease significantly until $x > 5.0\%$, which also marks the limit of meaningful d_{33} response in this study.

From the dielectric measurements alongside the crystallographic data in Figs. 1 and 4, d_{33} is maximum where the lattice parameters condense to a more pseudocubic structure, then drops sharply following the local re-emergence of tetragonal dominance at $x = 4.0\%$, prior to the rapid decline in (c_T/a_T) ratio with subsequent BZN additions. The d_{33} similarly declines sharply in the composition regime $4.0\% < x < 5.0\%$, despite a re-bound in the (c_T/a_T) at $x > 4.0\%$. This is consistent with the dielectric measurements and prior research[11] on the xBZN(1–x)BT system that $x = 5.0\%$ is the limit of ferroelectricity at 295 K.

3.4. *Polarization data*

Polarization loops and their corresponding E-J switching peaks are shown in Fig. 9.

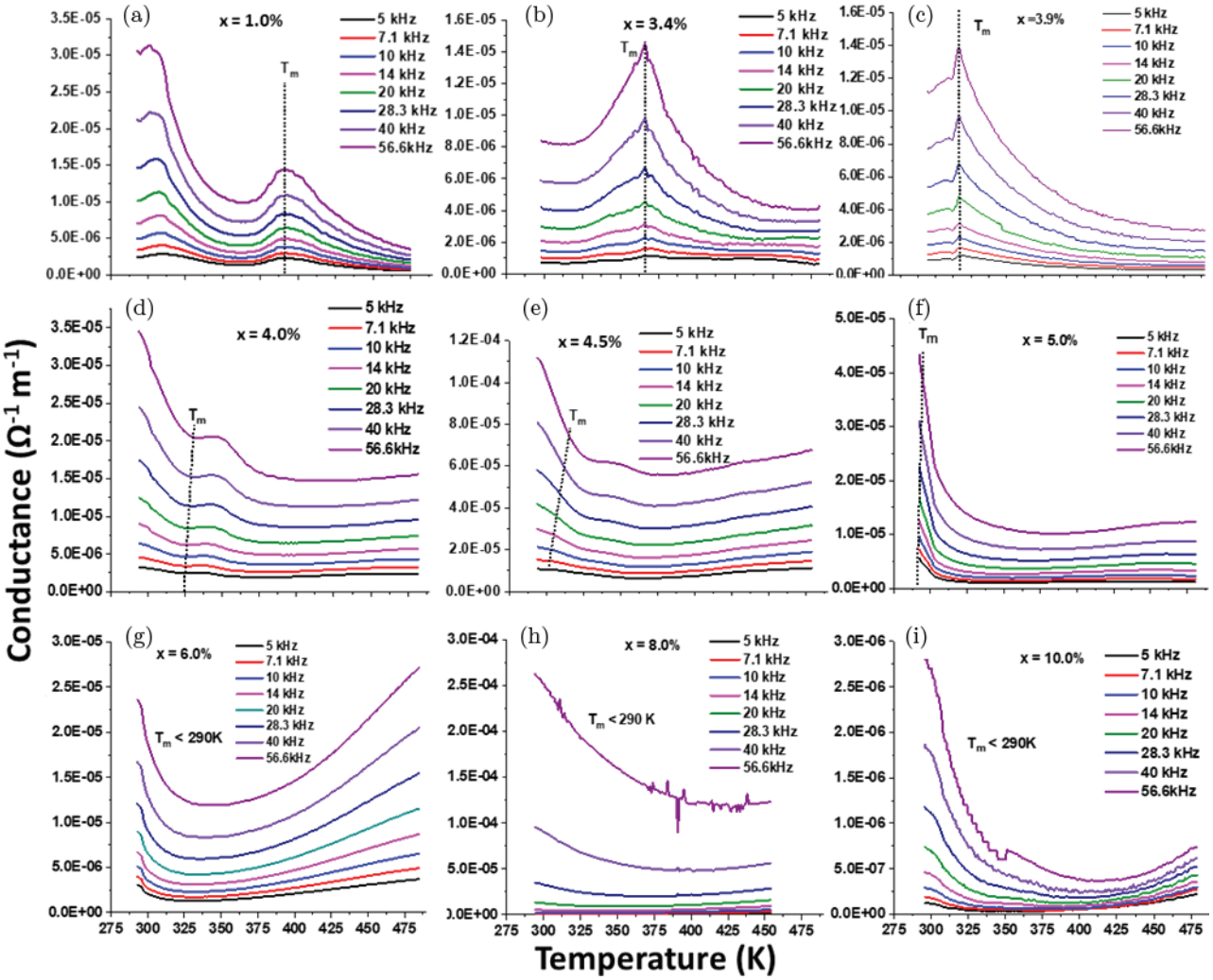

Fig. 7. Conductance for compositions (a) $x = 1.0\%$, (b) 3.4%, (c) 3.9%, (d) 4.0%, (e) 4.5%, (f) 5.0%, (g) 6.0%, (h) 8.0% and (i) 10.0%. $T_m < 290$ K for $6.0\% < x < 10.0\%$ at (640 kHz). Dotted line shows T_m with respect to conductance.

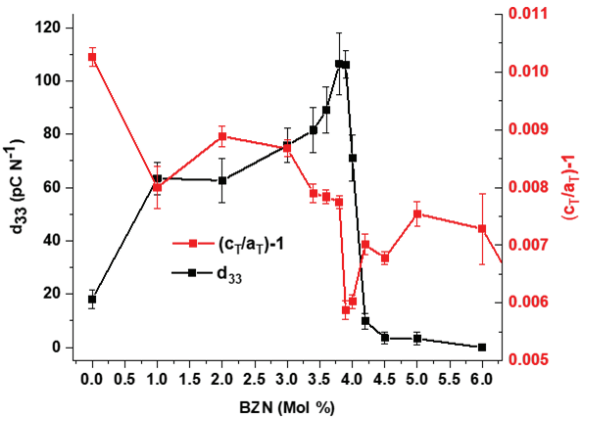

Fig. 8. Trends in d_{33} and $(c_T/a_T)-1$ with BZN concentration for measurable d_{33} coefficients.

BZN additions to $BaTiO_3$ increased the coercive field E_c, spontaneous polarization, P_s, and the remnant polarization, P_r up to $x = 3.9\%$. Polarization loops still show the classic "square" ferroelectric shape at $x = 4.0\%$, but the loops quickly lose their definition with subsequent BZN additions as seen in Fig. 9(f), alongside features within the current plots indicative of current leakage. No suitable loops were obtained for compositions $6.0\% < x < 7.0\%$ since the conductivity was too high to obtain data at applied electric fields greater than 0.5 kV cm^{-1}. The change in loop shape between $x = 4.0\%$ (Fig. 9(e)) and 4.5% (Fig. 9(f)) indicates that the onset of the ferroelectric-relaxor transition occurs at $4.0\% < x < 4.5\%$. The dispersive nature of the P-E loop at $x = 4.5\%$ is consistent with the highly dispersive dielectric properties shown in Fig. 6.

The composition at $x = 1.0\%$ shows slim hysteresis loops similar to those observed from $BaTiO_3$ ceramics in other

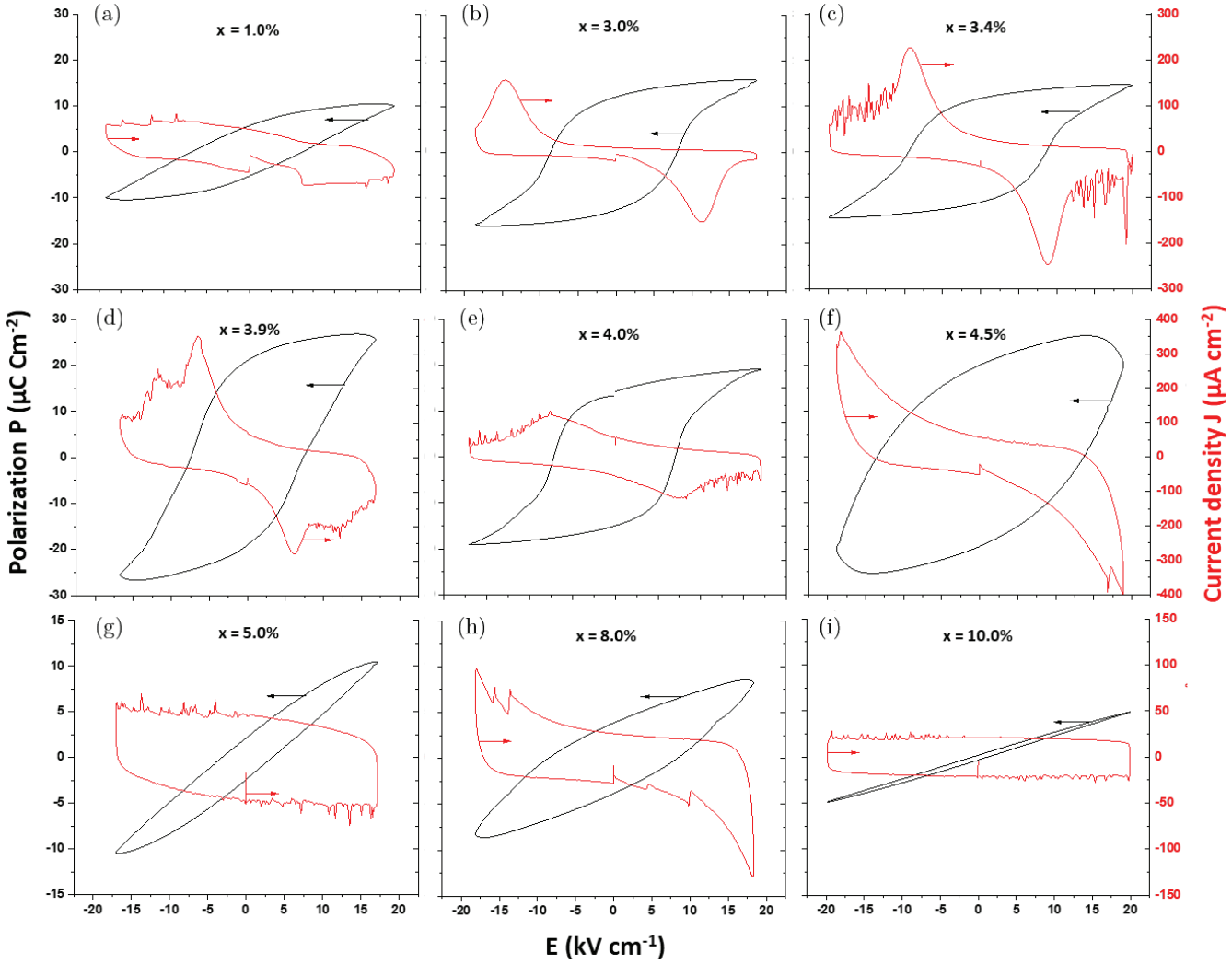

Fig. 9. Polarization and voltage current density loops from $BaTiO_3$ and BZNBT samples. (a) $x = 1.0\%$, (b) 3.0%, (c) 3.4%, (d) 3.9%, (e) 4.0%, (f) 4.5%, (g) 5.0%, (h) 8.0% and (i) 10.0%. Compositions $x > 4.0\%$ show the transition to lossy relaxor to low-loss dielectric relaxor at $x > 10.0\%$ onwards.

studies,[21,22] particularly for fine-grained ceramics. The low value of P_s is consistent with the small d_{33} obtained from $BaTiO_3$ relative to other studies[23] in that the ceramic processing methods in this work are not fully optimized with respect to grain size and dielectric properties.

The P-E loop at $x = 1.0\%$ shows small current peaks over a range of coercive fields, indicative of stepped domain switching consistent with the sloped P-E loops. In contrast, $x = 3.0\%$ shows a single, large current peak in current near E_c, as reflected by the wider P-E loop. Multiple peaks are seen with subsequent additions between $3.0\% < x < 4.0\%$ as seen in Figs. 9(b)–9(d), indicating 2–3 larger steps in domain switching relative to $BaTiO_3$-like compositions, defined here as $0 < x \leq 3.0\%$. The regime where multiple current peaks are present during switching is observed between $3.4\% < x \leq 3.9\%$, where the smaller discrete switching peaks seen at $x = 3.4\%$ (Fig. 9(b)) coalesce into 3 stepped peaks at 3.9%. The highest current density peak was also observed for $x = 3.9\%$, which also has the maximum values of P_r and P_s. For $x = 4.0\%$, the loops show the ferroelectric character but only one significant current peak evident and a decline in P_s and P_r relative to $x = 3.9\%$ is observed. This indicates that changes in domain switching occur at the onset of relaxation from 2–3 large steps to multiple discrete switching steps at E_c.

From the shape of the E–J loop in Fig. 9(f) at $x = 4.5\%$ in the relaxor ferroelectric regime, the position of the current peaks and the magnitude are more consistent with charge leakage than domain switching. The shape of the loop is anomalous relative to other compositions and resembles that of a lossy dielectric more than a relaxor ferroelectric. Sample dependency can be ruled out since these loops were obtained from multiple ceramic samples of the same composition.

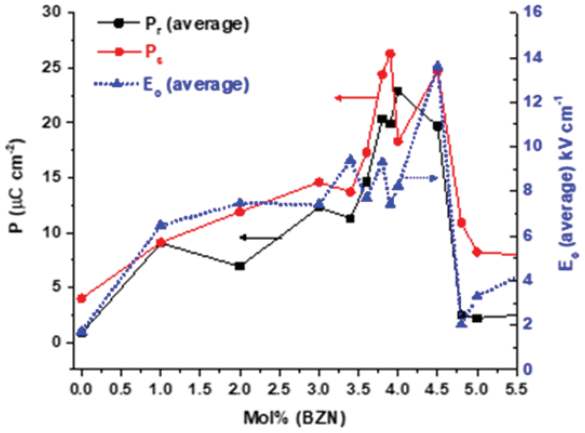

Fig. 10. Trends in P_r, P_s and E_c with BZN composition.

Charge leakage is much reduced for $x = 5.0\%$ (Fig. 9(g)) relative to $x = 4.5\%$ with small switching peaks for all values of applied field and a drop in E_c relative to compositions closer to $x = 4.0\%$. For $x > 5.0\%$, slimmer hysteresis loops characteristic of relaxor ferroelectrics are present,[11] with an exception at $x = 8.0\%$, consistent with the high dielectric loss observed for this composition.

Trends in remnant and spontaneous polarization (P_r and P_s) alongside coercive field up to $x \geq 5.0\%$ are shown in Fig. 10. The coercive field E_c plateaus around 8 kV cm^{-1} up to $x = 4.0\%$. An increase in E_c at $x > 4.0\%$ is observed with a maximum at $x = 4.5\%$, followed by a steep decrease at $x > 4.5\%$ in line with P_r and P_s. The average remnant polarization P_r more closely follows the trend in orthorhombic abundance and lattice parameters, than E_c, shown in Figs. 3 and 4, with a peak in P_r at $x = 4.0\%$ and a steep decline at $x > 4.0\%$. From Fig. 10 it is unclear whether the apparent increase in both E_c and P_s from $x = 4.0\%$ to $x = 4.5\%$ is a result of resistance to domain switching or an artifact from current leakage, since composition $x = 4.5\%$ is a highly lossy relaxor ferroelectric measured close to T_m as seen in Figs. 6 and 7. Composition $x = 8.0\%$ shows a similar P-E loop with V-J loops indicative of significant charge leakage. Subsequent addition of BZN reduced P_r, E_c and the current leakage, resulting in slim, low-loss relaxor dielectric loops, consistent with previous observations of this system.[11]

4. Conclusions

Dilute additions ($x < 10\%$) of $Bi(Zn_{2/3}Nb_{1/3})O_3$ (BZN) to $BaTiO_3$ resulted in considerable structural distortion to the $BaTiO_3$ host, with a significant impact on the dielectric properties within the xBZN(1–x)BT system. Initial additions ($1.0\% < x < 3.0\%$) of BZN to $BaTiO_3$ enabled stable *P4mm*/*Amm2* phase coexistence at room temperature, with *Amm2* presence dominating for $3.4\% < x < 3.9\%$. A well-defined ferroelectric-relaxor transition was observed in the region $4.0\% < x < 5.0\%$, characterized by (i) a local minima in tetragonal c_T/a_T ratio at $x = 3.9\%$; (ii) discontinuity in the orthorhombic/ tetragonal phase abundance at 295 K, (iii) onset of dielectric relaxation at T_m and appearance of the cubic phase at 295 K for $x \geq 4.0\%$ and (iv) decline in P_r and transition to relaxor dielectric from $4.0\% < x < 5.0\%$ onwards. Comparison of models incorporating either *Cm* as a polar phase or having *Pm-3m* present from $x = 1.0\%$ onwards indicate that the polar phases consist of *P4mm* and *Amm2* at 295 K for compositions $0 < x < 4.0\%$.

This work shows that there is a fundamental change in the electro-mechanical properties of the xBZN(1–x)BT at $x = 4.0\%$. This is reflected by the current peak no longer coinciding with T_m at $x \geq 4.0\%$ in Fig. 7 and the drop in d_{33} at $x \geq 4.0\%$ as shown in Fig. 8, even though the c_T/a_T at $4.0\% < x < 5.0\%$ is close to that at $x \leq 3.8\%$ and the dielectric constant remains high ($\varepsilon_m \geq 3000$) up to $x = 7.0\%$. The main observations from this study are summarized as follows:

(i) Dilute BZN additions stabilized the coexistence of the two polar *P4mm* and *Amm2* phases at 295 K. Orthorhombic *Amm2* dominated at 295 K for $3.4\% < x < 3.9\%$. Lack of asymmetry from (111) and (222) peaks indicate no non-90° angles within unit cells, hence no rhombohedral or monoclinic phase.

(ii) A crystallographic discontinuity near $3.8\% < x \leq 4.0\%$ is marked by the convergence of the lattice parameters of the polar phases at $x = 3.9\%$ (Fig. 4(a)). This is also reflected by peaks in ε_m, d_{33} and P_s and the de-coupling of peak conductance with T_m at $x \geq 4.0\%$.

(iii) Composition $x = 4.0\%$ marks the first appearance of the cubic phase as a trace at 295 K, where $T < T_m$ and a local maxima in *P4mm* intensity at $T < T_m$. Relaxor characteristics become established between $4.0\% < x < 5.0\%$.

(iv) Low-loss relaxor dielectric properties (Figs. 5 and 8) observed for compositions $x \geq 10.0\%$ up to miscibility limit at $x = 20.0\%$.

(v) Five main composition regimes are observed for the BZNBT system; (i) $0 < x < 3.0\%$ $BaTiO_3$-like ferroelectric; (ii) Stepped current-switching *Amm2*-dominant ferroelectric $3.4\% < x < 3.9\%$; (iii) Relaxor ferroelectric, characterized by the onset of dispersion and *Pm-3m* presence at $T < T_m$ for $4.0\% < x < 5.0\%$; (iv) Lossy relaxor dielectric $5.0\% < x < 10.0\%$ and (v) low loss relaxor dielectric $x > 10.0\%$.

Appendix A

Dielectric constant and loss for compositions $1.0\% < x < 10.0\%$

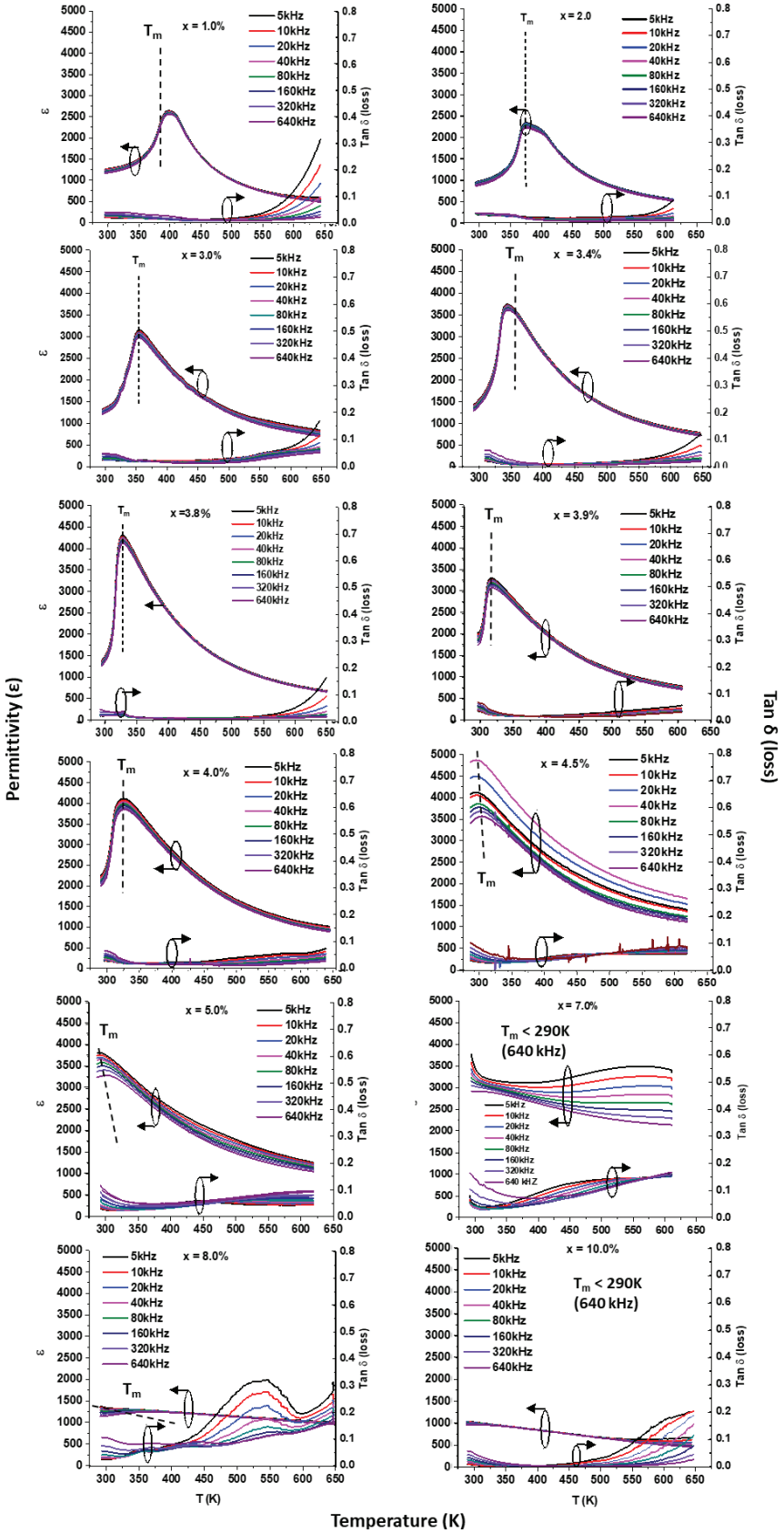

Appendix: Dielectric constant, T_m and loss for compositions $1.0\% < x < 10.0\%$ for frequencies 5 kHz–640 kHz.

Acknowledgments

The authors would like to thank the Department of Physics, Steven Huband and Mike Glazer for editorial and practical support.

The Panalytical MPD diffractometer used in this research was obtained through the Science City Energy Futures Project with support from Advantage West Midlands (AWM).

References

[1]L. E. Cross, Relaxor ferroelectrics, *Ferroelectrics* **76**, 241(1987).
[2]L. Wu, X. Wang and L. Li Lead-free $BaTiO_3$–$Bi(Zn_{2/3}\ Nb_{1/3})O_3$ weakly coupled relaxor ferroelectric materials for energy storage, *RSC Adv.* **6**, 14273 (2016).
[3]X. Chen *et al.,* Relaxor behavior and dielectric properties of $Bi(Zn_{2/3}Nb_{1/3})O_3$-modified $BaTiO_3$ ceramics, *J. Electron. Mater.* **44**, 4804 (2015).
[4]A. A. Bokov and Z. G. Ye, Recent progress in relaxor ferroelectrics with perovskite structure, *J. Mater. Sci.* **41**, 31 (2006).
[5]V. V. Shvartsman *et al.,* Crossover from ferroelectric to relaxor behavior in $BaTi_{1-x}\ Sn_x\ O_3$ solid solutions, *Phase Transit.* **81**, 1013 (2008).
[6]V. V. Shvartsman and D. C. Lupascu, Lead-free relaxor ferroelectrics, *J. Am. Ceram. Soc.* **95**, 1 (2012).
[7]S. Huband and P. A. Thomas, Depolarisation of $Na_{0.5}\ Bi_{0.5}\ TiO_3$-based relaxors and the resultant double hysteresis loops, *J. Appl. Phys.* **121**, 184105 (2017).
[8]M. Valant, Electrocaloric materials for future solid-state refrigeration technologies, *Prog. Mater. Sci.* **57**, 980 (2012).
[9]S. Nomura, K. Kaneta, J. Kuwata and K. Uchino, Phase transition in the $(1\text{-}x)PbTiO_{3-x}A(B_{2/3}Nb_{l/3})O_3$ solid solutions, *Mater. Res. Bull.* **17**, 1471 (1982).
[10]A. Paterson, H. T. Wong, Z. Liu, W. Ren and Z. G. Ye, Synthesis, structure and electric properties of a new lead-free ferroelectric solid solution of $(1\text{-}x)BaTiO_{3-x}Bi(Zn_{2/3}Nb_{1/3})O_3$, *Ceram. Int.* **41**, S57 (2015).
[11]L. Wu, X. Wang, Z. Shen, L. Li and A. Feteira, Ferroelectric to relaxor transition in $BaTiO_{3-x}Bi(Zn_{2/3}Nb_{1/3})O_3$ ceramics, *J. Am. Ceram. Soc.* **100**, 265 (2017).
[12]D. Wang *et al.*, Phase diagram and enhanced piezoelectric response of lead-free $BaTiO_3$-$CaTiO_3$-$BaHfO_3$ system, *J. Am. Ceram. Soc.* **97**, 3244 (2014).
[13]K. I. Othman *et al.,* Formation mechanism of barium titanate by solid-state reactions, *Int. J. Sci. Eng. Res.* **5**, 1460 (2014).
[14]R. Beanland and P. A. Thomas, Symmetry and defects in rhombohedral single-crystalline $Na_{0.5}Bi_{0.5}TiO_3$, *Phys. Rev. B — Condens. Matter Mater. Phys.* **89**, 1 (2014).
[15]N. Zhang *et al.,* The missing boundary in the phase diagram of $PbZr_{1-x}Ti_xO_3$., *Nat. Commun.* **5**, 1 (2014).
[16]A. M. Gonzalez, L. Pardo, M. E. Montero-Cabrera and L. E. Fuentes-Cobas, Analysis of the rhombohedral-tetragonal symmetries coexistence in lead-free 0.94 $(Bi_{0.5}Na_{0.5})TiO_3$-$0.06BaTiO_3$ceramics from nanopowders, *Adv. Appl. Ceram.* **115**, 96 (2016).
[17]W. Janbua, T. Bongkarn, T. Kolodiazhnyi and N. Vittayakorn, High piezoelectric response and polymorphic phase region in the lead-free piezoelectric $BaTiO_3$-$CaTiO_3$-$BaSnO_3$ ternary system, *RSC Adv.* **7**, 30166 (2017).
[18]R. A. Young, *The Rietveld Method* (Oxford University Press, 1993).
[19]B. H. Toby, R factors in rietveld analysis: How good is good enough?, *Powder Diffr.* **21**, 67 (2006).
[20]L. F. Zhu *et al.,* Enhanced piezoelectric and ferroelectric properties of $BiFeO_3$-$BaTiO_3$ lead-free ceramics by optimizing the sintering temperature and dwell time, *J. Eur. Ceram. Soc.* **38**, 3463 (2018).
[21]G. Chen *et al.,* Effects of sintering method and $BiFeO_3$ dopant on the dielectric and ferroelectric properties of $BaTiO_3$–$BiYbO_3$ based solid solution ceramics, *Ceram. Int.* **44** (2018), doi:10.1016/j.ceramint.2018.06.126.
[22]D. Ghosh *et al.,* Domain wall displacement is the origin of superior permittivity and piezoelectricity in $BaTiO_3$ at intermediate grain sizes, *Adv. Funct. Mater.* **24**, 885 (2014).
[23]T. Hoshina *et al.,* Domain size effect on dielectric properties of barium titanate ceramics, *Jpn. J. Appl. Phys.* **47**, 7607 (2008).